

In-situ metallic coating of atom probe specimen for enhanced yield, performance, and increased field-of-view

Tim M. Schwarz^{1*}, Eric Woods¹, Mahander P. Singh¹, Chanwon Jung¹, Leonardo S. Aota¹, Kyuseon Jang¹, Mathias Krämer¹, Se-Ho Kim^{1,3}, Ingrid McCarroll¹, Baptiste Gault^{1,2*}

1. Max-Planck-Institut für Eisenforschung, Max-Planck-Str. 1, Düsseldorf 40237, Germany
2. Department of Materials, Imperial College London, London, SW7 2AZ, UK
3. *now at* Department of Materials Science and Engineering, Korea University, Seoul 02841, Republic of Korea

*Corresponding author E-mail address: tim.schwarz@mpie.de, b.gault@mpie.de

ORCID:

Tim M. Schwarz: <https://orcid.org/0000-0001-9348-4160>

Eric Woods: <https://orcid.org/0000-0002-1169-893X>

Mahander P Singh: <https://orcid.org/0000-0003-1784-7219>

Chanwon Jung: <https://orcid.org/0000-0002-9782-0261>

Leonardo S. Aota: <https://orcid.org/0000-0002-1520-2073>

Kyuseon Jang: <https://orcid.org/0000-0003-1826-7443>

Mathias Krämer: <https://orcid.org/0000-0002-1352-9064>

Se-Ho Kim: <https://orcid.org/0000-0003-1227-8897>

Ingrid McCarroll: <https://orcid.org/0000-0002-0584-4769>

Baptiste Gault: <https://orcid.org/0000-0002-4934-0458>

Keywords: atom probe tomography; coating; mass resolution; yield; field of view

1 Abstract

Atom probe tomography requires needle-shaped specimens with a diameter typically below 100 nm, making them both very fragile and reactive, and defects (notches at grain boundaries or precipitates) are known to affect the yield and data quality. The use of a conformal coating directly on the sharpened specimen has been proposed to increase yield and reduce background. However, to date, these coatings have been applied ex-situ and mostly are not uniform. Here, we report on the controlled focused ion beam in-situ deposition of a thin metal film on specimens immediately after specimen preparation. Different metallic targets e.g. Cr were attached to a micromanipulator via a conventional lift-out method and sputtered using the Ga or Xe ions. We showcase the many advantages of coating specimens from metallic to non-metallic materials. We have identified an increase in data quality and yield, an improvement of the mass resolution, as well as an increase in the effective field-of-view enabling visualization of the entire original specimen, including the complete surface oxide layer. The ease of implementation of the approach makes it very attractive for generalizing its use across a very wide range of atom probe analyses.

2 Introduction

Atom probe tomography (APT) is a microscopy and microanalysis technique that provides three-dimensional compositional mapping^{1–3}. APT is underpinned by the field evaporation of surface atoms⁴. A field in the range of 10–100 V/nm is generated by applying a high voltage on the order of a few kilovolts to a needle-shaped specimen, with an end radius in the range of 20–100 nm. Superimposed to this electrostatic field are either high-voltage pulses⁵ or laser pulses^{6,7} that enable time-control of the field evaporation and hence time-of-flight measurement for each ion. Conversely to most other microscopy techniques, the specimen also acts as the primary ion projection optics^{8–10}, and control over its shape is hence critical to achieve optimal operation of the atom probe. Specimens can be prepared by electrochemical polishing^{11,12} or, as increasingly common, by lifting out a piece of the sample, depositing it onto a support and milling it into an appropriate shape using a dual beam scanning-electron microscope / focused-ion beam (SEM-FIB)¹³.

Needle-shaped substrates have been used as a support to deposit single or multiple layers of a range of materials and enable direct APT analysis. This approach has been particularly useful to study materials that were otherwise difficult to prepare into sharp needles, including carbon-based materials for instance^{14–16}, a range of metallic multilayers for studying diffusional and interfacial processes^{17–20}, along with glasses²¹ and thin organic layers^{22,23} or even frozen liquids^{24–26}. The deposition of thin metallic layers on silicon^{27,28}, ceramics²⁹ or glass³⁰ was shown to modify the field evaporation behavior, and for laser-pulsed atom probe tomography, it changes the light absorption and heat conduction properties of the specimen. These parameters are critical, since they control the rise and decay time of the “thermal pulse” that triggers field evaporation following laser pulse illumination^{31–34}, and hence the achievable performance limits of atom probe microanalysis.

Coating of APT specimens has been reported for ex-situ sputtering, i.e. following transfer through ambient atmosphere of specimens from the SEM-FIB to an external chamber for sputtering³⁵, by using physical-vapor³⁶, chemical-vapor deposition³⁷ (PVD & CVD, resp.) or atomic-layer deposition (ALD)^{38,39}. Encapsulation of thin layers of liquid by using graphene conductive coating have also been proposed^{40,41}. These coatings were shown to lead to improvements in mass resolution and yield⁴², with the

coating material and thickness being noted to have some influence on the results^{30,43}. The improvement in yield has been posited to be due to pores being filled⁴⁴, as these are known to result in early specimen fracture, likely due to stress concentration^{45,46}.

Coatings on flat substrates have also been used to encapsulate nanomaterials⁴⁷, e.g. nanoparticles^{48,49}, nanowires^{50,51} or nanosheets⁵² prior to performing the atom probe specimens. Shadowing effects during deposition, or the chemistry of the deposited material, i.e. the Pt-containing precursor in the FIB⁵³, or the use of an electrochemical potential that can affect the material to be deposited⁵⁴, can however make the analysis and interpretation arduous.

Recently, Woods et al.⁵⁵ revisited an approach introduced by Kölling et al.⁵⁶ at cryogenic temperatures to coat specimens directly in-situ in the SEM-FIB. This method used material sputtered by the ion beam from the surface of a piece of metal placed in the vicinity of the already sharpened specimen. Douglas et al. also showed how this in-situ sputtering could be used to strengthen the interface between a lifted-out sample and the Si-support⁵⁷, which proved critical to the yield for specimens prepared at cryogenic temperatures. This approach allows the precise control over which a section of the specimen's surface is coated and presents the advantage of being versatile with respect to the deposited material and the thickness of the coating.

Here, we report a more systematic study on the influence of these coatings on the final atom probe results. We demonstrate coating using Cr, Ti, Al, In, Bi, Co and Ag on a Ga-FIB and/ or a Xe-plasma FIB. The coating materials were deposited on a range of metallic and non-metallic atom probe needles. We report on the composition and structure of the coating itself, and its multiple beneficial effects on the atom probe analysis, including increased yield, increased mass resolution, reduced background levels in laser pulsing mode, and an increased field of view. Ways forward with this approach are discussed for future possible generalization of the approach.

3 Methods

3.1 Materials

For this study, we selected a range of materials, which will be described in the relevant sections below. The targets used for in situ sputtering were typically small pieces of pure metals (99.99 %) either sourced from Goodfellow, Fisher Scientific GmbH or

mixed leftover from the synthesis of larger ingots at the Max-Planck-Institut für Eisenforschung. The metal pieces were first cut into small 3x7 mm pieces and ground and polished to create a flat surface and remove any oxidation products. Afterwards, the metal pieces were mounted on a SEM stub or the copper clip from Cameca Instrument Inc..

3.2 FIB-based coating

To highlight the versatility of the approach, multiple SEM-FIBs were used to prepare specimens, a Helios 600i, a Helios 5 CX Ga SEM-FIB, and a Xe-plasma FIB-SEM Helios PFIB (all Thermo-Fischer Scientific, Hillsboro, OR, USA). The latter two instruments are equipped with EZLift tungsten micromanipulators, with the Helios 5 manipulator having cryogenic capabilities, whereas the 600i is equipped with an Omniprobe micromanipulator.

Lamella preparation

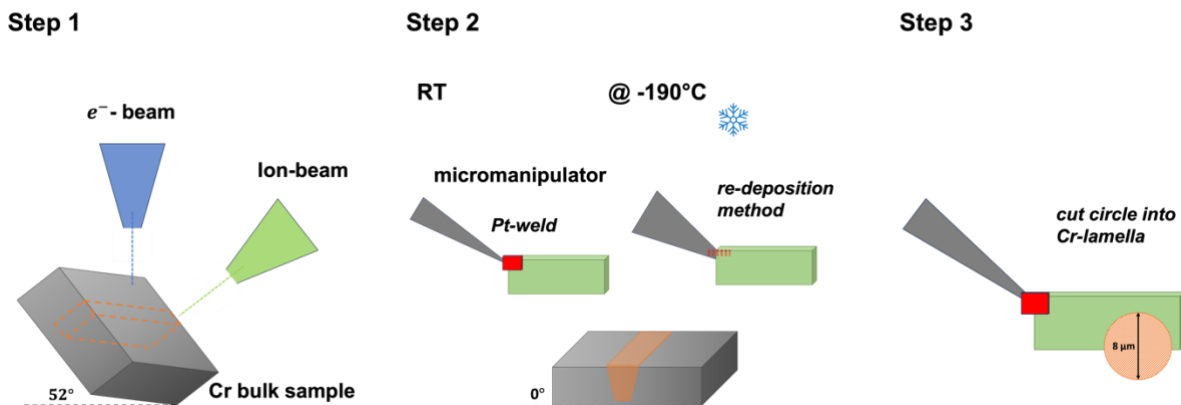


Figure 1: Schematic view of the target preparation.

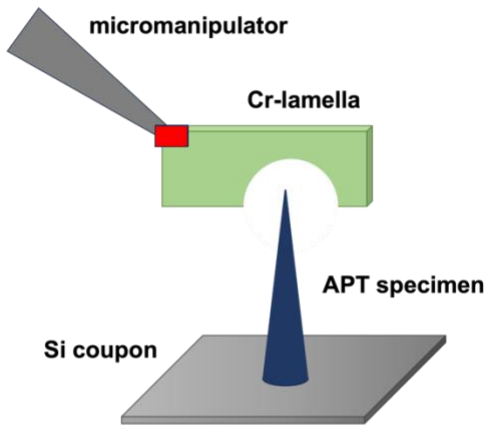
Figure 1 summarizes the lift-out procedure as described by Thompson et al.⁵⁸: a lamella of the metal to be deposited is lifted out and attached to the micromanipulator, Step 1. This can be done either by welding using the gas injection systems (GIS) or by re-deposition, under cryogenic temperatures^{55,59}, Step 2. A semi-circular opening with an 8–10 μ m diameter is then cut, Step 3.

Coating of APT specimen

A


Step 1 – Alignment

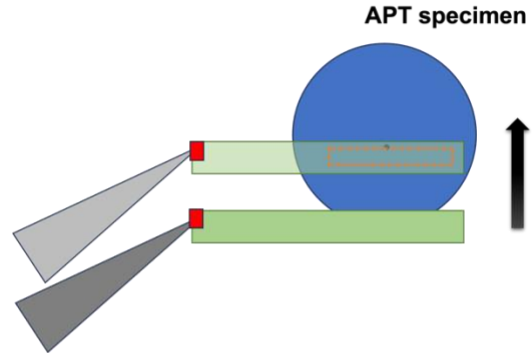
 Ion- beam



B

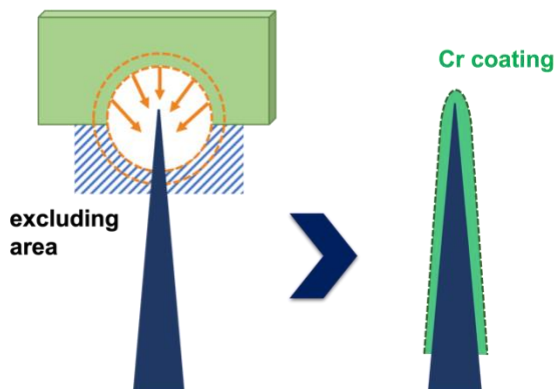
Step 2 – Alignment

 e^- - beam



C

Step 3 – Sputtering



D

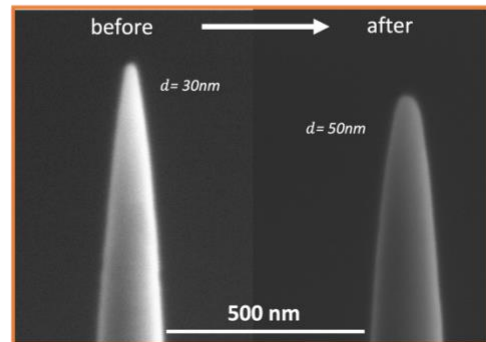


Figure 2: Schematic of the different steps for in-situ coating of samples in the FIB. Step 1 shows the positioning of the lamella in the ion beam in such a way that the specimen is in the center of the opening. In Step 2, the alignment in the electron beam is shown, where the top view of the specimen is represented by the blue circle, while the arrow indicates the movement of the manipulator to bring the target to the desired position. In Step 3, the ion beam is screened in the orange areas, while the blue area represents the exclusion zone. SEM images before and after coating a Ni tip with Cr are shown.

Figure 2 details the steps for the coating itself. The opening in the lamella is placed over a sharpened APT specimen, so that it sits directly in the center of the opening as imaged by the ion beam, Step 1. The bottom edge of the opening circle is typically about $1.5\ \mu\text{m}$ from the specimen's tip. The distance to the tip and the diameter of the circle will determine how much of the specimen is coated. For the electron beam, the lamella is placed in such a way that the sharpened specimen is covered by the upper

edge of the lamella Step 2. Finally, the ion beam is rastered on the metal target, from the inner circle outwards, using the pattern shown in orange in Figure 2, Step 3. To ensure that the beam does not hit the sample itself, an exclusion zone in the FIB is covered by the blue shaded area. The parameters used depend on the material being sputtered and the desired film thickness. For Cr, sputtering was performed at 30 kV and 40 pA for 30 seconds. To ensure a homogeneous and uniform coating from all sides, this process was repeated from four sides by rotating the specimen 90°, after each pass. Figure 2D shows an example of a Cr coated Ni specimen, before and after coating. At this scale, the coating appears in the form of a homogeneous and show a uniform increase in diameter of the specimen.

In addition to coating needle-shaped samples, it is also possible to coat the surfaces of flat samples. Protection layers deposited using the Pt-precursor from the GIS are generally not perfectly dense and contain carbon residues from the precursor gas, which can then cause issues during imaging by transmission-electron microscopy, and often make field evaporation in the APT of this layer problematic. When deposited with the ion beam, there can also be structural damage in the sub-surface region⁵⁸. With the method described in Figure 3, a metallic layer can be deposited *in-situ* on the desired location of the sample's surface. The lamella is moved close to the surface and the ion beam is rastered over the rectangular area marked in orange. The same parameters were used as for the needle-shaped specimen, but a longer deposition time of 1-4 min was required. In both cases, the coating can be done under cryo-conditions, making this method very versatile. Using the GIS under cryo-conditions is problematic because the gas condenses on all cold surfaces, which makes a controlled deposition impossible. Using this method, a thin metal layer can be deposited under cryo-conditions in a controlled manner.

Coating of a flat surface:

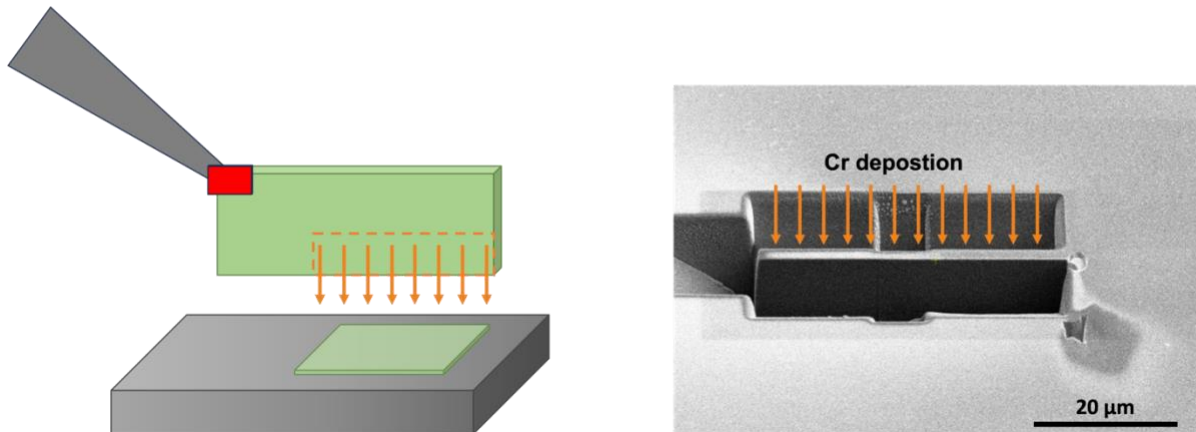


Figure 3: Schematic overview of the coating of a flat surface and the SEM image showing the coated surface.

3.3 APT

Following preparation and coating, specimens were either transferred through air or via cryo/vacuum suitcase (Ferrovac) to a Cameca LEAP 5000XS (straight flight path) or 5000XR (reflectron) atom probe. The specific running conditions will be specified below for each set of results. Data reconstruction and analysis were performed using APSuite 6.3 software. The initial reconstruction was performed using the measured start radius and angle of the specimen obtained from the SEM image of the sharpened/coated specimen, following the point projection protocol by Geiser et al.⁶⁰. The reconstruction parameters, image compression factor (ICF) and field factor (k_f) were calibrated using crystallographic poles as described in Gault et al.⁶¹ and adjusted to obtain lattice spacing, as reported in the literature.

3.4 (S)TEM

For the transmission electron microscope (TEM) analysis, a FEI Titan Themis microscope with an image corrector operated at 300 kV was used to reveal the structure of the in-situ metallic coating of a Ni specimen. Energy-dispersive X-ray (EDX) analyses and high- angle annular dark field (HAADF) imaging was performed in scanning TEM (STEM) mode using the same instrument.

4 Results & discussions

4.1 Structure and composition of the coating

Specimens for APT were prepared using a Ga-FIB and a Xe-PFIB from nanocrystalline, high purity (99.99 %) Ni. The nanocrystalline layer is formed during severe deformation from grinding the pure Ni plate. The plate is then gently polished to facilitate preparation by FIB lift out, as outlined in Thompson et al.⁵⁸.

TEM and (S)TEM analyses were performed to study the structure and thickness of the deposited Cr layer. Figure 4A displays TEM images after only one side of coating, where a thin homogeneous layer has deposited on the Ni specimen. After coating the specimen in each pass and rotating it 90° four times to coat it from all sides, the deposited layer thickness is approx. 10 nm. This is consistent with our estimation from the SEM images, shown in (Figure 2). Interestingly, the Cr layer is conformal with the specimen, homogeneous and uniform over several hundred nanometers down the shank, as readily visible in Figure 4B. There seems to be no discernible shadowing effects or columnar growth of the sputtered layer, which have been previously reported in the literature¹³. EDX mapping in S(TEM) mode shows the Cr layer around the Ni needle, Figure 4C. Figure 4D is a close-up of a notch on the edge of the specimen. Following coating, the outer edge of the specimen is smooth and homogeneous, which is likely to reduce the stress localization, leading to increased mechanical stability of the specimen during analysis. At this stage, whether the sputtered layer is nanocrystalline or amorphous is difficult to unambiguously assess and it likely that the structure is dependent on many parameters such as substrate and target materials, ion beam acceleration voltage and current.

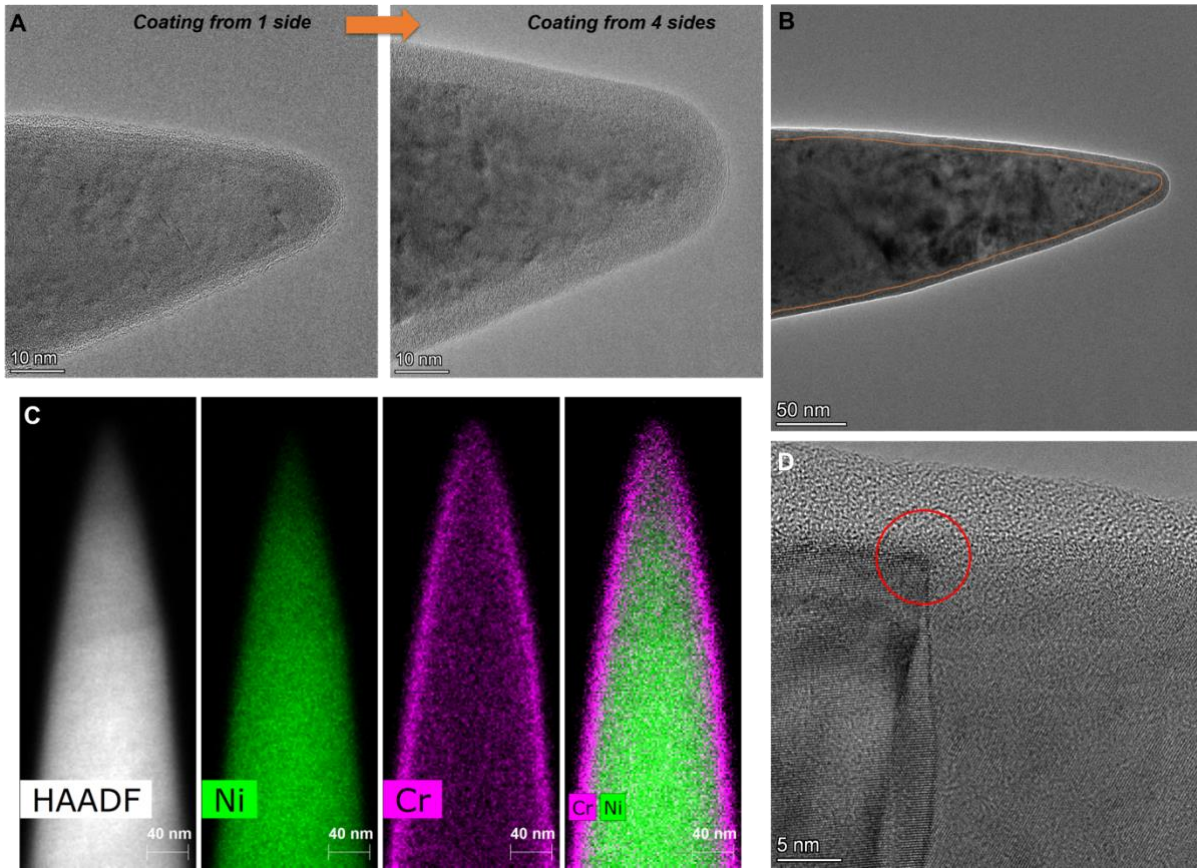


Figure 4: A shows a Cr coating on a Ni tip from one side and from four sides for comparison. B shows the tip with a homogeneous Cr layer of several hundred nanometers along the shaft of the tip. EDX mapping shows the Cr coating. Defects and roughness of the sample surface can be homogeneously coated, as shown here on the example of a grain boundary.

The chemical composition of the Cr-coating on a Ni specimen was then analyzed by APT following transfer through ambient conditions to the atom probe. Figure 5A and 5B display reconstructions of specimens prepared by Xe-PFIB and Ga-FIB, respectively. The coating covers the top and sides of the specimen. The Xe and Ga distributions are visualized using iso-surfaces. Xe tends to agglomerate, whereas Ga appears distributed across the entire Cr layer. The composition of the Cr layer varies strongly, with 53.5 at % Cr, 45.9 at. % O and 0.6 at. % Xe obtained on the PFIB (Table 1). This contrasts with the composition of the coating obtained by Ga-FIB that is 85.3 at. % Cr, 8.5 at. % oxygen and 6.2 at. % Ga (see Table 1).

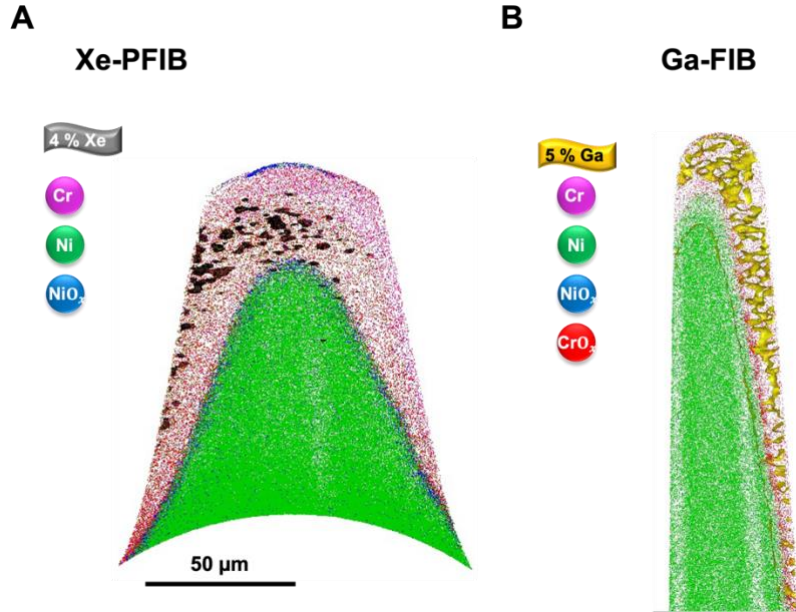


Figure 5: Comparison of the structure of the Cr layer produced with a Xe and a Ga FIB. In A the Xe clusters with an iso-surface concentration of 4 at.% and in B the Ga distribution with an iso-surface concentration of 5 at.% are visualised.

Table 1: Composition of the Cr coating prepared by a Xe and Ga FIB. All numbers are given in at.%.

	Xe-PFIB	Ga-FIB
Ga	-	6.241
Xe	0.593	-
Cr	53.506	85.241
O	45.897	8.518

Oxygen originates from the fast formation of the passivating Cr-oxide in between two passes of the ion beam on the surface. The difference in composition could result from differences in vacuums achieved in the two microscopes, or from the fact that the Xe removes ions mostly from the surface, which is likely to be more enriched in oxygen. In general, a higher Ga content is observed compared to Xe, which can be attributed to its higher reactivity, deeper penetration, and overall higher concentration of Ga inside of the target material compared to Xe.

4.2 Yield and mechanical resistance

Atom probe specimen from the same nanocrystalline Ni were prepared and Cr-coated using a Ga-FIB (Helios 5 CX). APT analyses were performed at 50 K, in laser pulsing mode (laser pulse energy of 40 pJ), with a repetition rate of 200 kHz and with an average detection rate of 1.5 ion per 100 pulses for both uncoated and Cr-coated specimens. The voltage curve from an analysis of an uncoated specimen is plotted in Figure 6A. It exhibits multiple dips, marked with blue arrows in Figure 6A, that are related to instabilities in the detection rate that can be attributed to sudden changes in the specimen's shape or the loss of fragments of the specimen⁶². Multiple specimens were analyzed. In each case the specimen fractured before 6 million ions could be collected. After coating, the voltage dips are no longer observed, as can be seen from the voltage curve in Figure 6b. For three analyzed specimens, the analysis was stopped when a set voltage of 8 kV was reached, and for each 60–100 million ions were collected without specimen fracture occurring.

We attribute this increase in yield to more stable field evaporation conditions. The high density of grain boundaries in nanocrystalline materials makes them particularly susceptible to such problems. The Cr coating appears to smooth the surface roughness out, and fill in some of the notches or pores, as observed by TEM in Figure 4D, thereby explaining the improved field evaporation conditions. Mechanical stabilization and the associated improvement in yield of coated samples was observed here for a range of material systems – from nanocrystalline metals to oxides, to biominerals – and is in agreement with previous work^{42,56}.

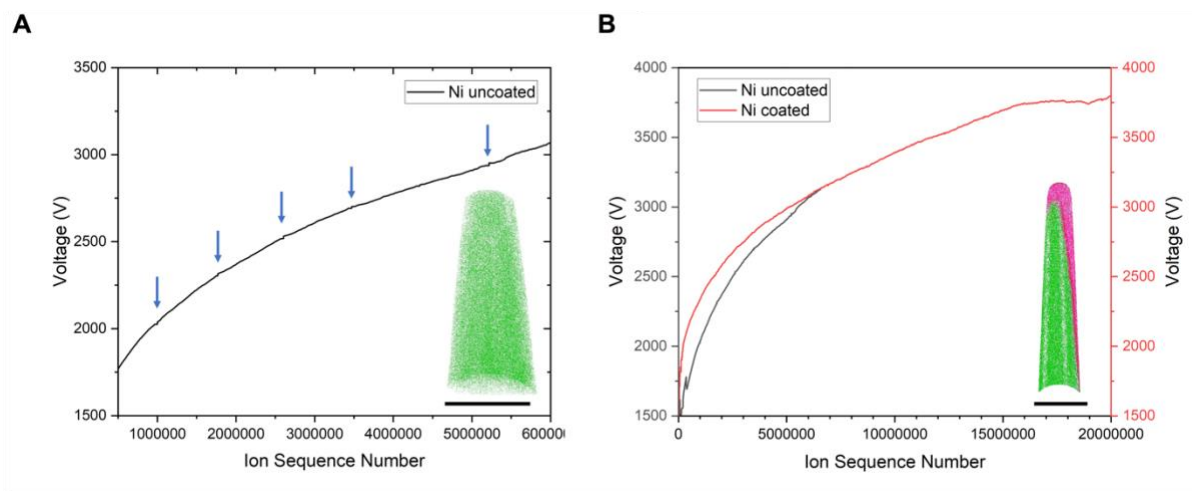


Figure 6: In A, the voltage curve for the uncoated Ni sample shows several dips, indicating uneven evaporation due to GB or other defects and inhomogeneities. B

compares the voltage curve for the uncoated and coated Ni samples, showing a monotonous increase for the coated sample with no noticeable dips.

4.3 Mass spectrum improvements

Improvement in the mass resolution and background levels with a thin metallic coating of poor thermally conducting specimen have previously been reported^{29,42}. Here, a small fragment from the dentine of a tooth of an unidentified dinosaur found in South Korea was analyzed by APT on a LEAP 5000 XR. APT analyses were performed at 50 K, in laser pulsing mode (laser pulse energy of 60 pJ), with a repetition rate of 100 kHz and with an average detection rate of 1.0 ion per 100 pulses for both uncoated and Cr-coated specimens. Specimens were prepared on a Ga-FIB (Helios 600i) using the protocol in Thompson et al.⁵⁸. It is well known that minerals, such as teeth, which consist mainly of Mg and other inorganic elements, have poor thermal properties, and therefore tend to form more pronounced thermal tails during APT analysis^{63,64}. This leads to a loss of information related to impurities and trace elements that may be indistinguishable due to large thermal tail. To investigate the influence of the Cr coating on improving thermal conductivity, some dentine samples were coated with Cr and others were not. Figure 7 shows a section of the mass spectrum obtained from the analysis of a non-coated sample (blue) with over 11×10^6 ions and a coated sample (red) with over 21×10^6 ions. Both spectra have been normalized to the $^{40}\text{Ca}^{2+}$ -peak at 20 Da.

In the uncoated samples, the long thermal tail of the $^{40}\text{Ca}^{2+}$ peak leads to a considerable overlap with the peaks of the other Ca isotopes. The thermal tailing spreads over a long area, indicating poor thermal conductivity of the material. Such long tailings can make the identification and quantification of trace elements impossible. It is also difficult to identify isotope ratios, which can be critical in quantifying data when there are overlapping peaks and for the dating of fossils and minerals⁶⁵. The shape of the Ca peak is typical for minerals obtained from a dozen analyses of the same material.

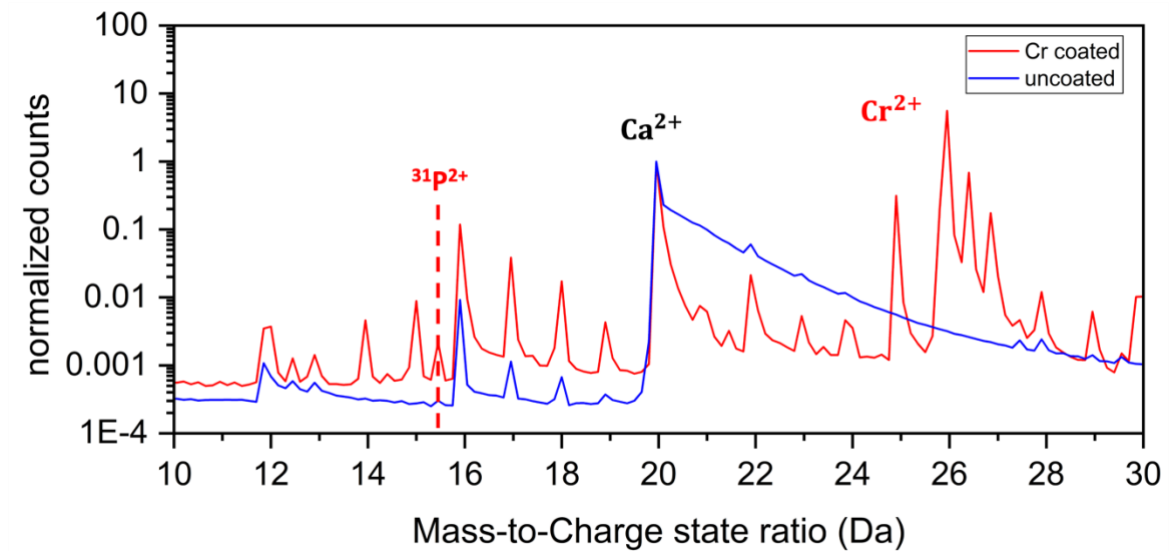


Figure 7: Normalized mass spectra to the Ca-peak for a coated (red) and uncoated (blue) specimen prepared from the dentine of a fragment of an unidentified dinosaur tooth.

In the case of the Cr-coated specimen, the mass resolution is vastly improved and peak separation greatly simplified. This enables the detection of peaks otherwise hidden, for instance $^{31}\text{P}^{2+}$ at 15.5 Da, and more accurate isotopic ratio measurements: for the uncoated specimen the $^{40}\text{Ca}^{2+}$ peak represents only less than 72 %, whereas it is 94.9 % for the coated specimen, noting that the natural abundance is 96.9 %. We did not perform specific quantification of the improvement in mass resolution or background level since the specimen shape still varies from specimen to specimen, even over the course of a single analysis.

4.4 Effect on the field-of-view: analysis of aluminum

4.4.1 Pure-Al analyses

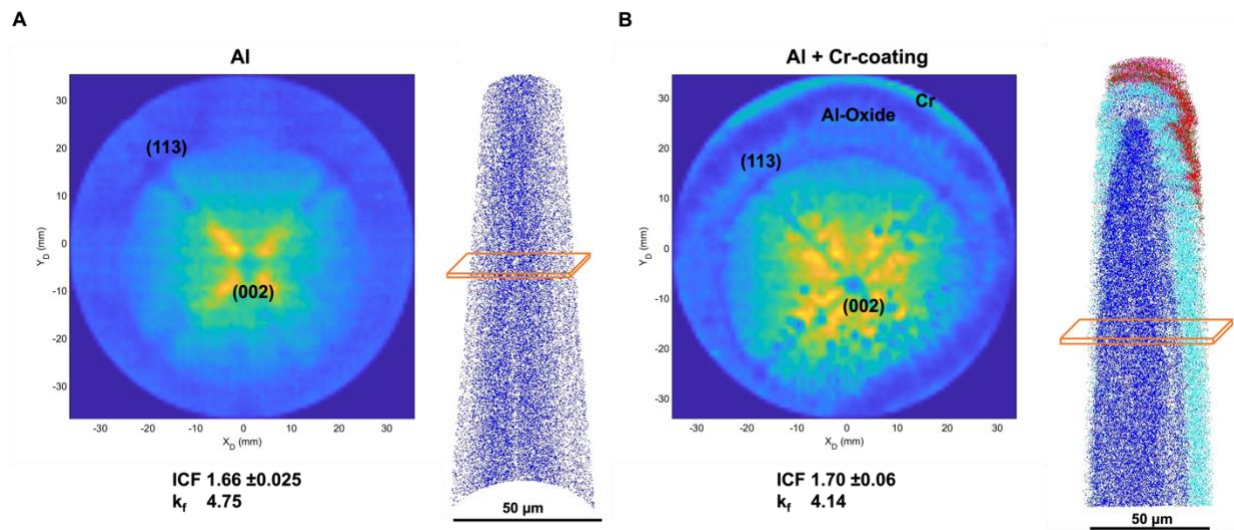


Figure 8: A: data for the uncoated Al specimen clearly shows the (002) and (113) poles in the detector hit maps, along with the 3D reconstruction; B, the Cr coated Al specimen shows the same poles in the Al-core, and the passivating surface oxides around the specimen indicates a larger field of view. The extracted area for the desorption map is marked with an orange parallelepiped.

To investigate the effect on the field-of-view and possible changes in the image compression factor (ICF), specimens were prepared from a pure Al plate, ground and polished to remove surface oxides. Specimens from both samples were prepared using the Xe-PFIB to minimize any spurious effect of Ga implantation on the visibility of crystallographic poles. To accurately determine the change in image compression factor and field-of-view, while avoiding the influence of different radii or shank angles from specimen to specimen, we first measured 8 million ions from a specimen, then performed the Cr-coating. The APT analyses were performed at 50 K, in laser pulse mode (laser pulse energy of 40 pJ), with a repetition rate of 200 kHz and an average detection rate of 1.5 ions per 100 pulses. The same parameters were used for the uncoated and Cr-coated samples to aim for consistent measurement conditions. Figure 8 A and 8B report on data obtained on the pure Al specimen before and after coating respectively. Since the specimen transfer from the atom probe into the FIB was done in ambient atmospheric condition, a thin oxide layer has formed, as visible in Figure 8B.

To study a native oxide on an APT sample it is necessary to capture the first thousands of atoms from the tip apex. This can be very challenging due to alignment requirements

and due to their tendency to fracture off prior to reaching the metal/oxide interface. Here, after Cr-coating, the native oxide layer on the tip apex and along the shank of the specimen can be analyzed, leading to a massive increase in square nanometers of analyzable oxide/metal interface data. The capability of studying the surface of the atom probe tip is significant for any research group studying surface catalytic or oxidation and could lead to a higher success rate and throughput in the future. The thickness of the natural oxide layer on Al was measured to be between 6-8 nm, which is in good agreement with literature values⁶⁶.

4.4.2 Effect on the reconstruction parameters

Both detector hit maps show clear crystallographic poles. The ICF depends on the theoretical and observed crystallographic angles between two poles⁶⁷. Poles pertaining to the (002) and the four variants of the (113) planes were used to calculate the ICF, which is 1.66 ± 0.025 and a calculated k_f of 4.75 following calibration. After coating the same specimen with Cr, Figure 8B, the ICF was calculated using the same poles when visible, and it was 1.70 ± 0.06 , with a k_f of 4.14 determined from adjusting the (002) plane spacing at a depth of approx. 150 nm into the Al.

The field evaporation of the surface atoms results in a progressive increase in the tip's radius that typically results in a decrease in k_f and ICF^{68,69}. Here, the decrease in k_f can be explained by the increase in the specimen's radius due to the coating^{68,69}. However, contrary to the expectation that the ICF should drop with increasing radius^{68,69}, we see no significant change in the ICF after the Cr coating has been evaporated from the top and the Al core is being analyzed – maybe a slight additional compression of the field lines and therefore of the ion trajectories arising from the presence of the Cr coating, but no severe distortions towards the interface between the metal and the coating.

4.4.3 Origins of the increased field-of-view

A striking difference following coating is the analysis of the native oxide on the specimen's shank, which indicates a significant increase in the imaged surface area at the specimen, despite a limited change in angular compression, i.e. the ICF is almost constant, as illustrated in Figure 9. There are two important factors here. First is the angular field-of-view, that is typically between ± 25 – 30° about the specimen's main axis, and that relates to the angular compression of the trajectory reflected by

the ICF. Second, this angular field-of-view defines the actual field-of-view that is the imaged area at the specimen's surface shown by the red arc in Figure 9A, and that corresponds to the reverse projection of the detector onto the emitting specimen. As the radius increases because of the field evaporation during the APT analysis, the imaged surface area also increases, leading to a total analyzed volume delineated by the thick red lines.

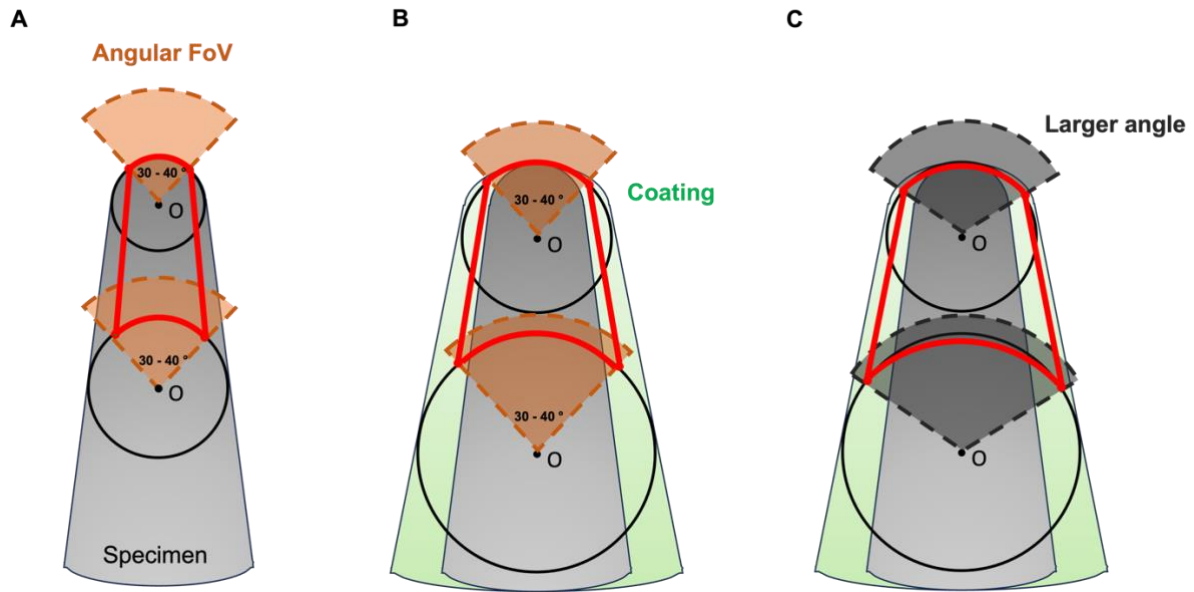


Figure 9: (A) Schematic view of the angular field-of-view of an uncoated sample, in red is delineated the analyzed volume by APT; (B) the coating makes the specimen thicker, thereby increasing the imaged surface area at the specimen's tip, even with a constant angular compression; (C) a larger angular field-of-view arising from a change in the ICF would simply make the field-of-view mildly wider.

Coating the specimen is equivalent to increasing its radius. Even if the angular field-of-view (i.e. ICF) remains the same, as in Figure 9B, the imaged surface area increases, allowing for imaging the sides of the original specimen. A similar increase in the imaged surface could arise from an increased angular field-of-view, Figure 9C, yet this would have translated into a strong change in ICF, which was not measured experimentally. The application of this thin Cr-coating appears to lead to an increased field-of-view similar to the use of an electrostatic lensing system^{70,71}. The use of the conventional reconstruction algorithm did not lead to severe distortions on the edges of the field-of-view.

4.5 Effect on the field-of-view: precipitates in Al-alloy

We then perform a similar set of analyses on an Al-5.18Mg-6.79Li (at. %) alloy aged for 8h at 150°C to form spherical δ' -precipitates, for more details, please refer to Gault et al.⁷². Following grinding and polishing to remove surface oxides, specimens were prepared using the Xe-PFIB. APT analyses were performed at 50 K, in laser pulse mode (laser pulse energy of 20 pJ), with a repetition rate of 200 kHz and an average detection rate of 1 ion per 100 pulses for both the uncoated and Cr-coated samples.

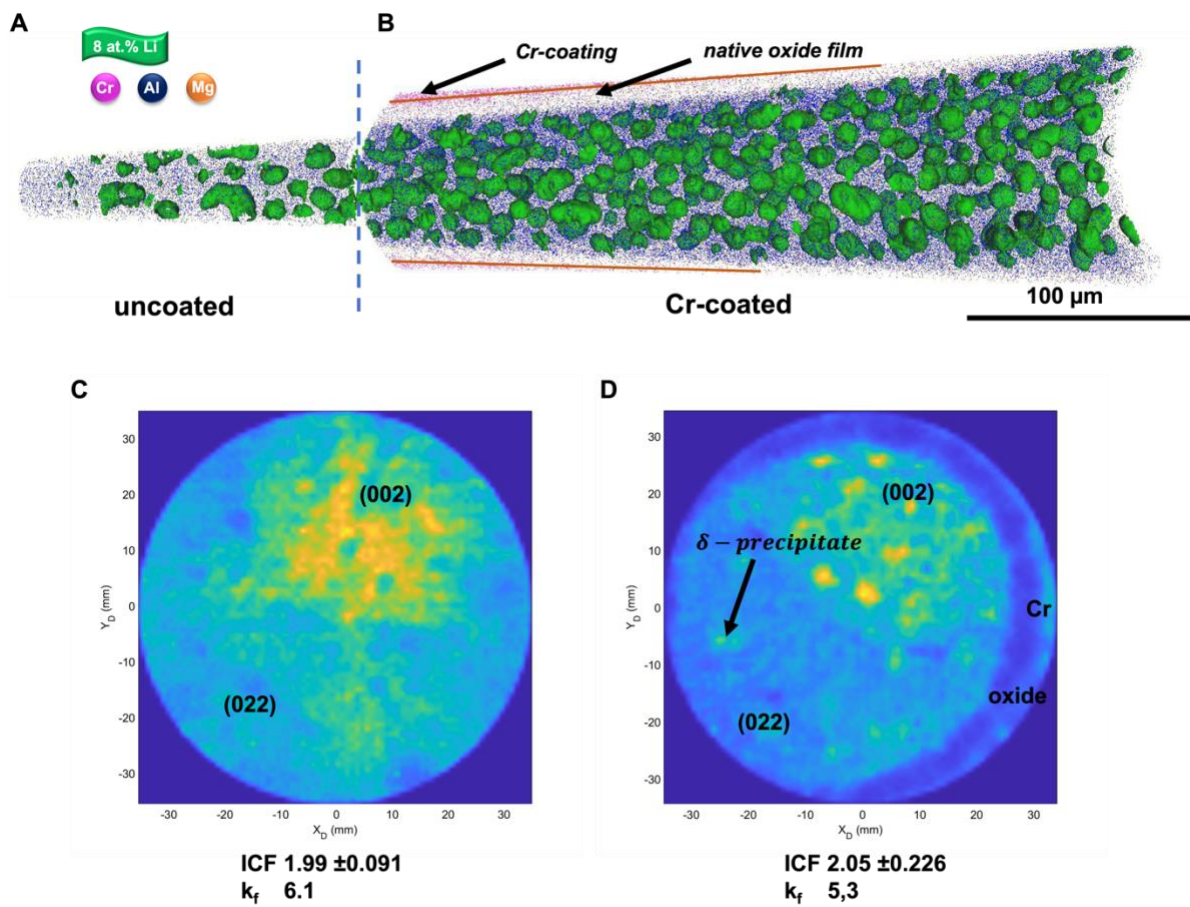


Figure 10: In A, a comparison between uncoated and coated samples, Li δ' -precipitates are visualized using an iso-surface concentration of 8 at.% Li. In the Cr-coated sample, the Cr layer and the naturally formed oxide layer can be seen, the interface between the two being highlighted by orange lines. C and D show the corresponding desorption maps for the coated and uncoated specimen.

Figure 10 is a 10-nm-thick slice through the combined reconstructions obtained from the analysis of the same specimen uncoated, Figure 10A, and Cr-coated, Figure 10B. The ICF was determined using the two poles marked in Figure 10 C and D, and the k_f factor was calculated by adjusting the spacing of the (002) planes. Like the pure Al specimen discussed above, no significant change in the ICF is observed. The increase

in field-of-view offered by the Cr-coating allows for imaging the native oxide and part of the Cr layer itself, with the Cr/native oxide interface indicated by orange lines. It also leads to a substantial increase in the number of precipitates imaged through the specimen's cross section. This increase in the number of analyzed precipitates for a single specimen can help improve statistical accuracy, and it is also possible to analyze larger precipitates that may not be directly in the center of the sample. These were also highlighted as advantages arising from the use of the lensing system in other instrument design^{70,71}, but were achieved on a conventional atom probe geometry through this thin metallic coating.

4.6 Discussion

4.6.1 Perspective on the benefits of coatings

Several effects of an in-situ deposited metallic coating on APT specimens were reported, including improved mechanical resistance, better thermal conductivity, and an increase in the field-of-view. It is interesting to note that the ICF does not change significantly, indicating only a small additional compression of the field lines. A major advantage of this method is that no additional instrumentation is required, and the coating can be deposited in any FIB, with a Ga or Xe source and under cryogenic conditions.

In addition, the coating of the samples allows the complete oxide layer around the tip to be seen, as well as the Cr layer, thus allowing the outer layer and the thickness of the oxide layer to be analyzed. In comparison to the recently released Invizo instrument, which can analyze the outer oxide layer formed on specimens, Tegg et al. reported that only a maximum detection area of 90% could be reached⁷¹, making the assessment of the oxide layer thickness challenging, whereas the Cr-coating acts as a clear marker.

It was also reported that the lensing system used to increase the field-of-view in the Invizo instrument leads to severe distortions in the reconstruction⁷¹. These are related to strong compression of the field lines and trajectories that are not appropriately taken into consideration in the currently available algorithms based on a point-projection model, making accurate reconstruction difficult. Cr coating does not lead to a significant change in the compression, meaning that current reconstruction algorithms

remain applicable, and no noticeable change or distortions of the spherical δ' -precipitates can be observed in Figure 10.

4.6.2 Limitation

With the coating imaged only on one side, in Figure 8B, the estimated ICF appears to be higher by 6% between the (002) and (113) pole marked in the figure, compared to between the (002) and the two (113) poles located on the perpendicular zone axis. Differences in the compression for specimen that do not exhibit cylindrical symmetry had previously been reported⁷³, which would lead to slight distortions in the reconstructed data since a single ICF is assumed across the field-of-view. The presence of the coating on one side could be due to a slight misalignment during the deposition process, or the specimen bending slightly, as was sometimes observed when thin specimens when they are too thin (see Fig. S1 for Al) or simply to a slight misalignment of the specimen in the LEAP. This does not appear to be related to the location where the laser hits the specimen (bottom left in the detector hit map).

From the detector hit maps after the Cr coating, Figure 8B, many areas of higher and lower event density appear, forming a speckled pattern indicative of overheating of the specimen from the laser. This observation suggests that the absorption of laser energy by Cr in the UV region (355 nm) is significantly higher than that of pure Al. Therefore, more energy is absorbed in the form of thermal energy which heats the Al sample significantly³³. Several publications have reported that Cr exhibits photoexcitation, which contribute to the higher sample temperature^{74,75}. The presence of the oxide layer around the Al, and the multiple interfaces can also limit the heat flows away from the apex.

There can also be severe interference in the mass spectrum between peaks from the materials being analyzed, the coated metal and its possible oxides - the APT analysis of Cr oxides shows many series of peaks up to relatively high mass-to-charge ratios⁷⁶. This is readily visible in Figure 7, but can be avoided by extracting the Cr-free region as a separate reconstruction in the analysis software. However, it is currently unclear whether sputtered metal reacts with the surface of the original specimen, or the underlying native oxide, or if the deposition process causes structural damage.

4.6.3 Future considerations

Our coating approach is versatile, and many parameters can be optimized. For example, the coated metal can be chosen to match the evaporation field of the coated material to minimize the evaporation field contrast and possible resulting aberrations. This might be even more critical when running in voltage pulsing mode, as field evaporation contrast may lead to a build-up of stresses at the interface and facilitate fracture, or simply create additional aberrations.

There are many possibilities for the metal to be coated, and it is easy to change the target, but the deposited metal must adhere sufficiently and not react with the incident ion beam. In this respect, the choice of an element with only one or two isotopes, with relatively well-defined oxides, or with a low tendency to form oxides, or with high atomic masses, may seem optimal. Noble metals such as Ag, Pt, Pd or Au could also avoid possible reactions with the surface.

For each material, suitable sputtering parameters must first be found and optimized in the FIB, but this process offers the possibility of using a wide range of metals. Ti, In, Bi, Al, Co and Ag have also been tried out with similar deposition parameters (see Figure S2-S7).

The Ag layer was very inhomogeneous and will require future optimization. Nevertheless, the mass spectrum of the Ag-coating layer shows promising behavior as at lower mass-to-charge state ratios than Ag peaks, only Ga and two unidentified peaks appear. At higher masses, several Ag oxide peaks appear, which may also be related to the speckled texture and its non-uniform evaporation behavior (Figure S3). For In, the reaction with the incident Ga ions from the primary beam resulted in an uneven deposition from a possibly liquid source, as the In-Ga alloy (42,6 (In) /52,4 (Ga) at.%) system ⁷⁷ has a low temperature eutectic (see Figure S4). This could be optimized by using the Xe-PFIB.

Similar observations were made for Al, where the Ga content in the sputtered layer was approx. 2.17 ± 0.33 , but the deposited layer was very homogeneous and uniform. This effect could be avoided by using Xe PFIB and Al is a promising candidate for a low evaporation material for coatings (Figure S2). The two candidates that have so far shown good sputtering properties with the same parameters are Ti, which has 5 isotopes and is therefore not perfect (Figure S7). Another candidate is Co, which also

forms a uniform layer and has only one isotope, making it attractive for coating, but the evaporation field is higher than all the other materials used (Figure S6).

Finally, the energy distribution of the deposited atoms or secondary ions emitted by the target is primarily undetermined at this stage, and so is how these ions possibly affect the specimen's surface upon deposition – i.e. causing implantation or structural damage to the surface and subsurface layers. Adjusting the energy of the primary Ga or Xe beam may be a lever to adjust this, to minimize damage from these secondary particles.

5 Summary & conclusions

To summarize, we have demonstrated a low-cost and fast method to form a conformal coating on APT specimens that appears homogeneous and uniform. The method uses in-situ sputtering of a metallic target by the FIB. This approach is versatile and leads to many benefits including:

- (i) environmental protection during transfer between the FIB and the atom probe, which is critical for studies of e.g. surfaces and reactive materials;
- (ii) a higher sample yield, possibly due to the mechanical stabilization provided by the coating;
- (iii) improved mass resolution and background level leading to improved sensitivity by a better thermal conductivity of and or better absorption of the laser energy by the metallic coating;
- (iv) possibilities to image the shank of the specimens, which dramatically increases the surface area of e.g. native oxides formed on atom probe specimens and further stabilization of the oxide layer evaporation;
- (v) the possibility to detect larger numbers of precipitates due to a larger field of view within the same specimen, thus increasing the throughput and statistical power and decreasing the number of runs and lower the cost;
- (vi) among other things, increasing the field of view by increasing the radius of the original tip does not compress the field lines, so the existing reconstruction algorithm is retained.

Much remains to be explored, such as optimizing the sputtering parameters and their influence on the thickness or crystalline structure of the coating, adapting the

sputtering parameters to different target materials, the influence of the coating on non-conductive or poorly thermally conductive materials, or the influence of the electrical and thermal conductivity of the target metal on analytical performance.

Declaration of Competing Interest

The authors declare that they have no known competing financial interest or personal relationships that could have appeared to influence the work reported in this paper.

Acknowledgments

Uwe Tezins, Andreas Sturm and Christian Broß are acknowledged for their support to the FIB & APT facilities at MPIE. TS, IM, EW, BG are grateful for funding from the DFG through the award of the Leibniz Prize 2020. IM, EW, BG are grateful for funding from the ERC – SHINE (771602). MK and BG acknowledge financial support from the German Research Foundation (DFG) through DIP Project No. 450800666. CJ is grateful for financial support from Alexander von Humboldt Foundation. KJ is grateful for funding from the Samsung Electro-Mechanics. SHK acknowledge the KIAT grant funded by the Korea Government MOTIE (P0023676).

6 References

1. Larson, D. J., Prosa, T. J., Ulfing, R. M., Geiser, B. P. & Kelly, T. F. Local electrode atom probe tomography. *N. Y. US Springer Sci.* 318 (2013).
2. Lefebvre-Ulrikson, Williams., Vurpillot, François. & Sauvage, Xavier. *Atom probe tomography : put theory into practice.* (Academic Press, 2016).
3. Gault, B. *et al.* Atom Probe Tomography. *Nat. Rev. Methods Primer* 1–51 (2021).
4. Forbes, R. G. Field evaporation theory: a review of basic ideas. *Appl. Surf. Sci.* **87/88**, 1–11 (1994).
5. Müller, E. W., Panitz, J. A., McLane, S. B. & Müller, E. W. Atom-Probe Field Ion Microscope. *Rev. Sci. Instrum.* **39**, 83–86 (1968).

6. Kellogg, G. L. & Tsong, T. T. Pulsed-laser atom-probe field-ion microscopy. *J. Appl. Phys.* **51**, 1184 (1980).
7. Bunton, J. H., Olson, J. D., Lenz, D. R. & Kelly, T. F. Advances in pulsed-laser atom probe: instrument and specimen design for optimum performance. *Microsc. Microanal. Off. J. Microsc. Soc. Am. Microbeam Anal. Soc. Microsc. Soc. Can.* **13**, 418–427 (2007).
8. Fortes, M. A. General properties of field-ion image projection. *Surf. Sci.* **28**, 117–131 (1971).
9. Cerezo, A., Warren, P. J. & Smith, G. D. W. Some aspects of image projection in the field-ion microscope. *Ultramicroscopy* **79**, 251–257 (1999).
10. De Geuser, F. & Gault, B. Reflections on the Projection of Ions in Atom Probe Tomography. *Microsc. Microanal.* **23**, 238–246 (2017).
11. Melmed, A. J. The art and science and other aspects of making sharp tips. *J. Vac. Sci. Technol. B* **9**, 601–608 (1991).
12. Miller, M. K. & Smith, G. D. W. *Atom Probe Microanalysis: Principles and Applications to Materials Problems*. (Materials Research Society, 1989).
13. Prosa, T. J. & Larson, D. J. Modern Focused-Ion-Beam-Based Site-Specific Specimen Preparation for Atom Probe Tomography. *Microsc. Microanal.* **23**, 194–209 (2017).
14. Southon, M. J., Boyes, E. D., Turner, P. J. & Waugh, A. R. Some applications of field-ionization and field-evaporation techniques in the study of surfaces. *Surf. Sci.* **53**, 554–580 (1975).
15. Prosa, T., Kostrna Keeney, S. & Kelly, T. F. Local electrode atom probe analysis of poly(3-alkylthiophene)s. *J. Microsc.* **237**, 155–167 (2010).
16. Zhang, S., Gervinskas, G., Liu, Y., Marceau, R. K. W. & Fu, J. Nanoscale coating on tip geometry by cryogenic focused ion beam deposition. *Appl. Surf. Sci.* **564**, 150355 (2021).

17. Balogh, Z., Reda Chellali, M., Greiwe, G.-H., Schmitz, G. & Erdélyi, Z. Interface sharpening in miscible Ni/Cu multilayers studied by atom probe tomography. *Appl. Phys. Lett.* **99**, 181902 (2011).
18. Larson, D. J., Cerezo, A., Juraszek, J., Hono, K. & Schmitz, G. Atom-Probe Tomographic Studies of Thin Films and Multilayers. *Mrs Bull.* **34**, 732–737 (2009).
19. Tamion, A., Cadel, E., Bordel, C. & Blavette, D. Three-dimensional atom probe investigation of Fe/Dy multilayers. *Scr. Mater.* **54**, 671–675 (2006).
20. Vovk, V., Schmitz, G., Hutten, A. & Heitmann, S. Mismatch-induced recrystallization of giant magneto-resistance (GMR) multilayer systems. *Acta Mater.* **55**, 3033–3047 (2007).
21. Greiwe, G.-H., Balogh, Z., Schmitz, G. & G-H Greiwe, Z. B., G. Schmitz. Atom probe tomography of lithium-doped network glasses. *Ultramicroscopy* **141**, 51–55 (2014).
22. Kelly, T. F., Nishikawa, O., Panitz, J. A. & Prosa, T. J. Prospects for Nanobiology with Atom-Probe Tomography. *Mrs Bull.* **34**, 744–749 (2009).
23. Nishikawa, O. & Kato, H. Atom-probe study of a conducting polymer: The oxidation of polypyrrole. *J. Chem. Phys.* **85**, 6758–6764 (1986).
24. Inghram, M. G. & Gomer, R. Massenspektrometrische Untersuchungen der Feldemission positiver Ionen. *Z. Für Naturforschung A* **10**, 863–872 (1955).
25. Anway, A. R. Field Ionization of Water. *J. Chem. Phys.* **50**, 2012–2021 (2003).
26. Stintz, A. & Panitz, J. A. Imaging Atom-Probe Analysis of an Aqueous Interface. *J. Vac. Sci. Technol. -Vac. Surf. Films* **9**, 1365–1367 (1991).
27. Jeske, T., Schmitz, G. & Kirchheim, R. Atom probe field ion microscopy investigation of the early interreaction stages in Al/Ni couples. *Mater. Sci. Eng. A* **270**, 64–68 (1999).
28. Schmidt, W. A., Melmed, A. J., Lovisa, M. F., Naschitzi, M. & Block, J. H. Field-ion energy spectroscopy of gold overlayers on silicon. *Surf. Sci.* **194**, 127–135 (1988).

29. Seol, J. B., Kwak, C. M., Kim, Y. T. & Park, C. G. Understanding of the field evaporation of surface modified oxide materials through transmission electron microscopy and atom probe tomography. *Appl. Surf. Sci.* **368**, 368–377 (2016).
30. Kellogg, G. L. Field ion microscopy and pulsed laser atom-probe mass spectroscopy of insulating glasses. *J. Appl. Phys.* **53**, 6383 (1982).
31. Houard, J., Vella, A., Vurpillot, F. & Deconihout, B. Optical near-field absorption at a metal tip far from plasmonic resonance. *Phys. Rev. B* **81**, 125411 (2010).
32. Houard, J., Vella, A., Vurpillot, F. & Deconihout, B. Three-dimensional thermal response of a metal subwavelength tip under femtosecond laser illumination. *Phys. Rev. B* **84**, 33405 (2011).
33. Vurpillot, F., Houard, J., Vella, A. & Deconihout, B. Thermal response of a field emitter subjected to ultra-fast laser illumination. *J. Phys. -Appl. Phys.* **42**, 125502 (2009).
34. Vurpillot, F., Gault, B., Vella, A., Bouet, M. & Deconihout, B. Estimation of the cooling times for a metallic tip under laser illumination. *Appl. Phys. Lett.* **88**, 94105 (2006).
35. Taylor, S. D. *et al.* Resolving Iron(II) Sorption and Oxidative Growth on Hematite (001) Using Atom Probe Tomography. *J. Phys. Chem. C* **122**, 3903–3914 (2018).
36. Kim, S. *et al.* Atom probe analysis of electrode materials for Li-ion batteries: challenges and ways forward. *J. Mater. Chem. A* **6**, 4883–5230 (2022).
37. Felfer, P., Benndorf, P., Masters, A., Maschmeyer, T. & Cairney, J. M. Revealing the distribution of the atoms within individual bimetallic catalyst nanoparticles. *Angew. Chem. Int. Ed Engl.* **53**, 11190–11193 (2014).
38. Li, Y., Zanders, D., Meischein, M., Devi, A. & Ludwig, A. Investigation of an atomic-layer-deposited Al₂O₃ diffusion barrier between Pt and Si for the use in atomic scale atom probe tomography studies on a combinatorial processing platform. *Surf. Interface Anal.* **53**, 727–733 (2021).
39. Mosiman, D. S. *et al.* Atom Probe Tomography of Encapsulated Hydroxyapatite Nanoparticles. *Small Methods* **5**, 2000692 (2021).

40. Adineh, V. R. *et al.* Graphene-Enhanced 3D Chemical Mapping of Biological Specimens at Near-Atomic Resolution. *Adv. Funct. Mater.* **28**, 1801439 (2018).
41. Exertier, F., Wang, J., Fu, J. & Marceau, R. K. W. Understanding the Effects of Graphene Coating on the Electrostatic Field at the Tip of an Atom Probe Tomography Specimen. *Microsc. Microanal.* 1–12 (2021) doi:10.1017/S1431927621012356.
42. Larson, D. *et al.* Improved mass resolving power and yield in atom probe tomography. *Microsc Microanal* **19**, 994–995 (2013).
43. Adineh, V. R. *et al.* Pulsed-voltage atom probe tomography of low conductivity and insulator materials by application of ultrathin metallic coating on nanoscale specimen geometry. *Ultramicroscopy* **181**, 150–159 (2017).
44. Barroo, C., Akey, A. J. & Bell, D. C. Aggregated nanoparticles: Sample preparation and analysis by atom probe tomography. *Ultramicroscopy* **218**, (2020).
45. Moy, C. K. S., Ranzi, G., Petersen, T. C. & Ringer, S. P. Macroscopic electrical field distribution and field-induced surface stresses of needle-shaped field emitters. *Ultramicroscopy* **111**, 397–404 (2011).
46. Wilkes, T. J. *et al.* Fracture of Field-Ion Microscope Specimens. *J. Phys. -Appl. Phys.* **5**, 2226–2230 (1972).
47. Larson, D. J. *et al.* Encapsulation method for atom probe tomography analysis of nanoparticles. *Ultramicroscopy* **159**, 420–426 (2015).
48. Felfer, P. *et al.* New approaches to nanoparticle sample fabrication for atom probe tomography. *Ultramicroscopy* **159**, 413–419 (2015).
49. Josten, J. P. & Felfer, P. J. Atom Probe Analysis of Nanoparticles Through Pick and Coat Sample Preparation. *Microsc. Microanal.* **28**, 1188–1197 (2022).
50. Prosa, T., Alvis, R., Tsakalakos, L. & Smentkowski, V. Analysis of Silicon Nanowires by Laser Atom Probe Tomography Prepared by a Protected Lift-Out Processing Technique. *Microsc. Microanal.* **14**, 456–457 (2008).
51. Lim, J. *et al.* Atomic-Scale Mapping of Impurities in Partially Reduced Hollow TiO₂ Nanowires. *Angew. Chem. - Int. Ed.* (2020) doi:10.1002/anie.201915709.

52. Kim, S.-H. S. H. *et al.* Direct Imaging of Dopant and Impurity Distributions in 2D MoS₂. *Adv. Mater.* **32**, (2020).
53. Perea, D. E., Gerstl, S. S. A., Chin, J., Hirschi, B. & Evans, James. E. An environmental transfer hub for multimodal atom probe tomography. *Adv. Struct. Chem. Imaging* **3**, 12 (2017).
54. Kim, S.-H. H. *et al.* A new method for mapping the three-dimensional atomic distribution within nanoparticles by atom probe tomography (APT). *Ultramicroscopy* **190**, 30–38 (2018).
55. Woods, E. V. *et al.* A versatile and reproducible cryo-sample preparation methodology for atom probe studies. Preprint at <https://doi.org/10.48550/arXiv.2303.18048> (2023).
56. Kölling, S. & Vandervorst, W. Failure mechanisms of silicon-based atom-probe tips. *Ultramicroscopy* **109**, 486–491 (2009).
57. Douglas, J. O., Conroy, M., Giuliani, F. & Gault, B. In Situ Sputtering From the Micromanipulator to Enable Cryogenic Preparation of Specimens for Atom Probe Tomography by Focused-Ion Beam. *Microsc. Microanal.* **29**, 1009–1017 (2023).
58. Thompson, K. *et al.* In situ site-specific specimen preparation for atom probe tomography. *Ultramicroscopy* **107**, 131–139 (2007).
59. Schreiber, D. K., Perea, D. E., Ryan, J. V., Evans, J. E. & Vienna, J. D. A method for site-specific and cryogenic specimen fabrication of liquid/solid interfaces for atom probe tomography. *Ultramicroscopy* **194**, 89–99 (2018).
60. Geiser, B. P. *et al.* Wide-Field-of-View Atom Probe Reconstruction. *Microsc. Microanal.* **15** (suppl), 292–293 (2009).
61. Gault, B. *et al.* Advances in the calibration of atom probe tomographic reconstruction. *J. Appl. Phys.* **105**, 034913 (2009).
62. Gault, B., Moody, M. P., Cairney, J. M. & Ringer, S. P. *Atom Probe Microscopy*. vol. 160 (Springer New York, 2012).
63. Gordon, L. M. & Joester, D. Nanoscale chemical tomography of buried organic-inorganic interfaces in the chiton tooth. *Nature* **469**, 194–197 (2011).

64. Gordon, L. M., Tran, L. & Joester, D. Atom probe tomography of apatites and bone-type mineralized tissues. *ACS Nano* **6**, 10667–10675 (2012).
65. Reddy, S. M. *et al.* Atom Probe Tomography: Development and Application to the Geosciences. *Geostand. Geoanalytical Res.* **44**, 5–50 (2020).
66. Evertsson, J. *et al.* The thickness of native oxides on aluminum alloys and single crystals. *Appl. Surf. Sci.* **349**, 826–832 (2015).
67. Gault, B. *et al.* Estimation of the Reconstruction Parameters for Atom Probe Tomography. *Microsc. Microanal.* **14**, 296–305 (2008).
68. Gault, B. *et al.* Dynamic reconstruction for atom probe tomography. *Ultramicroscopy* **111**, 1619–1624 (2011).
69. Loi, S. T., Gault, B., Ringer, S. P., Larson, D. J. & Geiser, B. P. Electrostatic simulations of a local electrode atom probe: the dependence of tomographic reconstruction parameters on specimen and microscope geometry. *Ultramicroscopy* **132**, 107–113 (2013).
70. Bostel, A. & Yavor, M. (12) Patent Application Publication (10) Pub. No.: US 2010/0223698 A1. **1**, (2010).
71. Tegg, L. *et al.* Characterising the performance of an ultrawide field-of-view 3D atom probe. *Ultramicroscopy* **253**, 113826 (2023).
72. Gault, B. *et al.* Atom probe tomography investigation of Mg site occupancy within delta' precipitates in an Al-Mg-Li alloy. *Scr. Mater.* **66**, 903–906 (2012).
73. Larson, D. J., Russell, K. F. & Miller, M. K. Effect of specimen aspect ratio on the reconstruction of atom probe tomography data. *Microsc. Microanal.* **5**, 930–931 (1999).
74. Al-Kuhaili, M. F. & Durrani, S. M. A. Optical properties of chromium oxide thin films deposited by electron-beam evaporation. *Opt. Mater.* **29**, 709–713 (2007).
75. Khalaf, M. K., Al-Kader, D. S. A. & Salh, J. M. Effect of thickness and type of substrate on optical properties of chromium oxide thin film prepared by sputtering magnetron. *IOP Conf. Ser. Mater. Sci. Eng.* **1105**, 012065 (2021).

76. La Fontaine, A. *et al.* Interpreting atom probe data from chromium oxide scales. *Ultramicroscopy* **159**, 354–359 (2015).
77. Anderson, T. J. & Ansara, I. The Ga-In (Gallium-Indium) System. *J. Phase Equilibria* **12**, 64–72 (1991).

7 Supporting Information

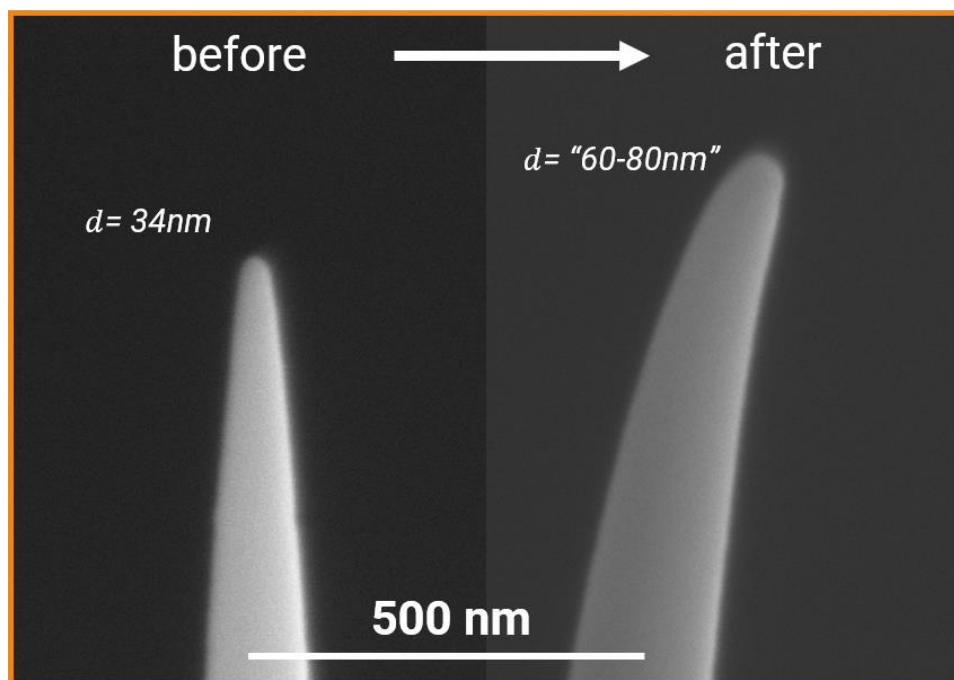


Figure S 1: Al sample before and after Cr-coating. The coating is uniform, and the radius of the original tip has increased but the tip is slightly bent.

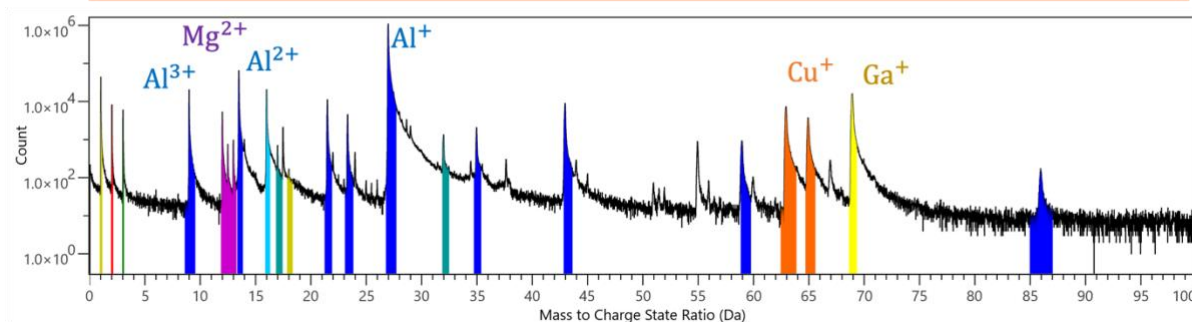
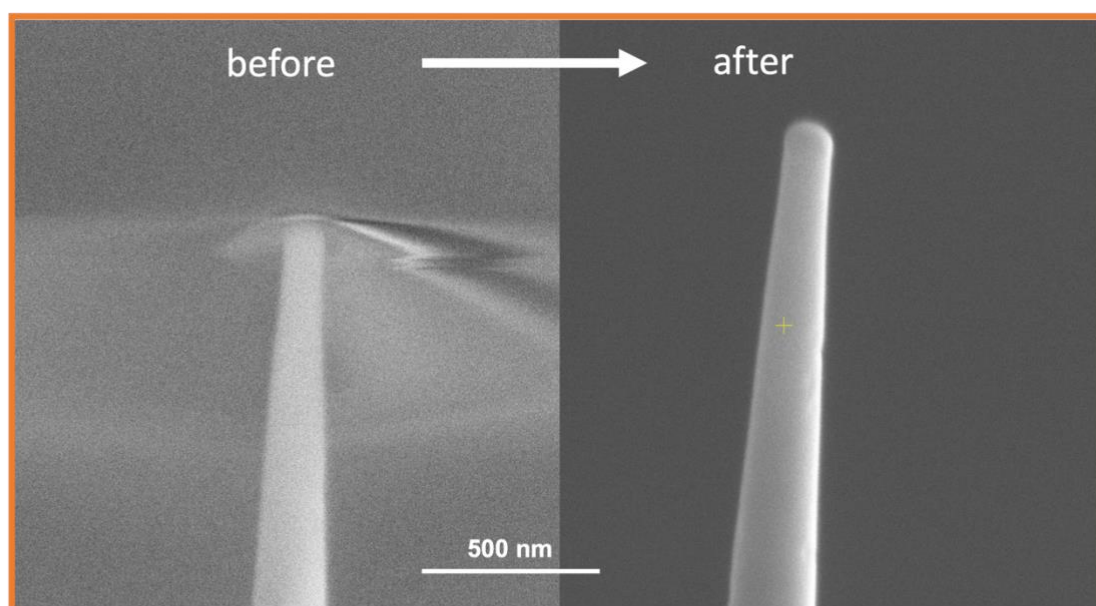


Figure S 2: Specimen coated with Al. The coating is uniform, the extracted mass spectra of the Al coating show some impurities (Mg and Cu) of the sputtered Al lamellae and several peaks of Al oxides.

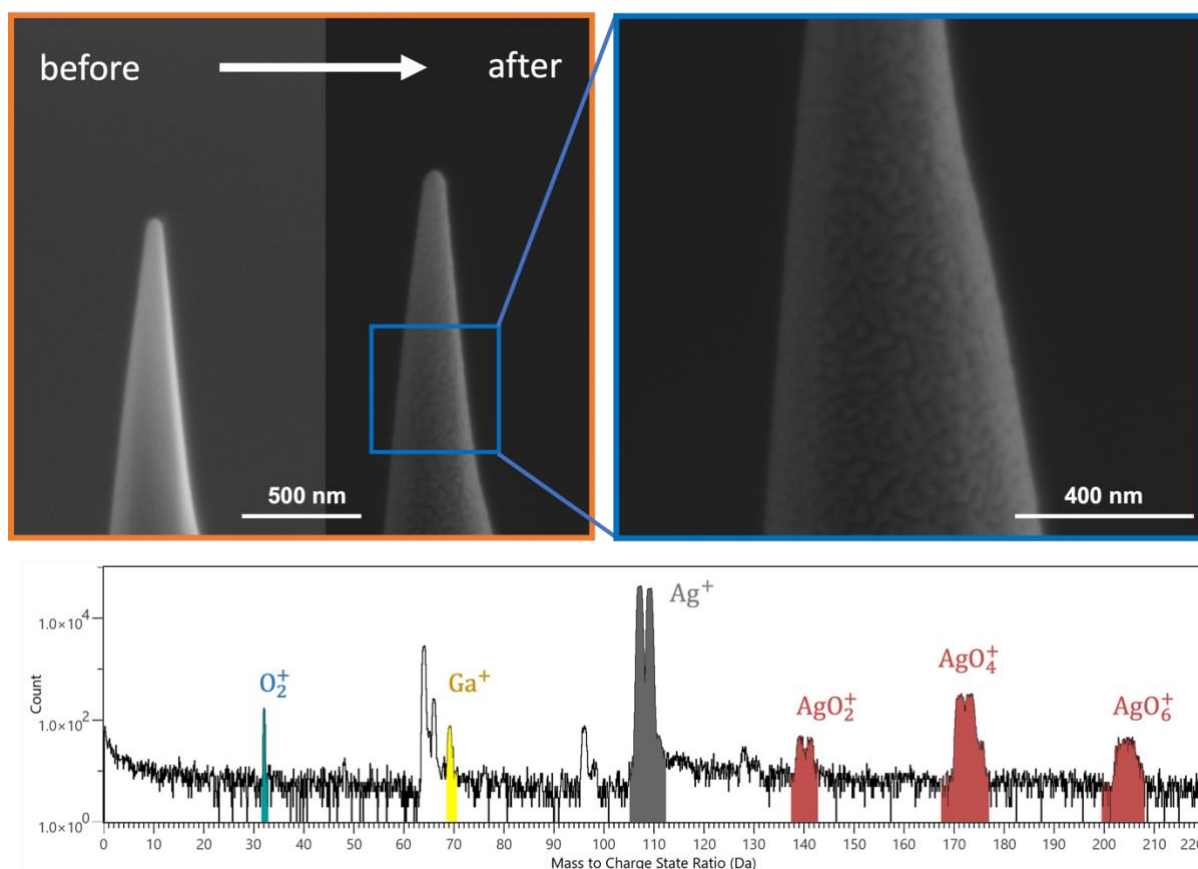


Figure S 3: Al specimen coated with Ag. The coating is not uniform and has a speckled texture. The mass spectrum of the Ag coating shows promising behavior as at low mass to charge state ratios only Ag-Ga and two unidentified peaks appear. At higher masses, several Ag oxide peaks appear, which may also be related to the speckled texture and its non-uniform evaporation behavior.

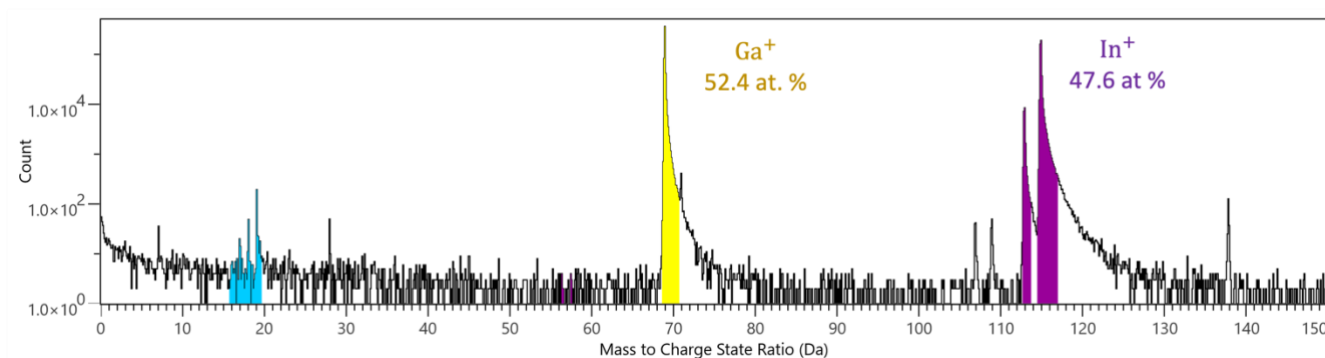


Figure S 4: Mass spectrum of the coated In layer, reveals a high proportion of Ga.

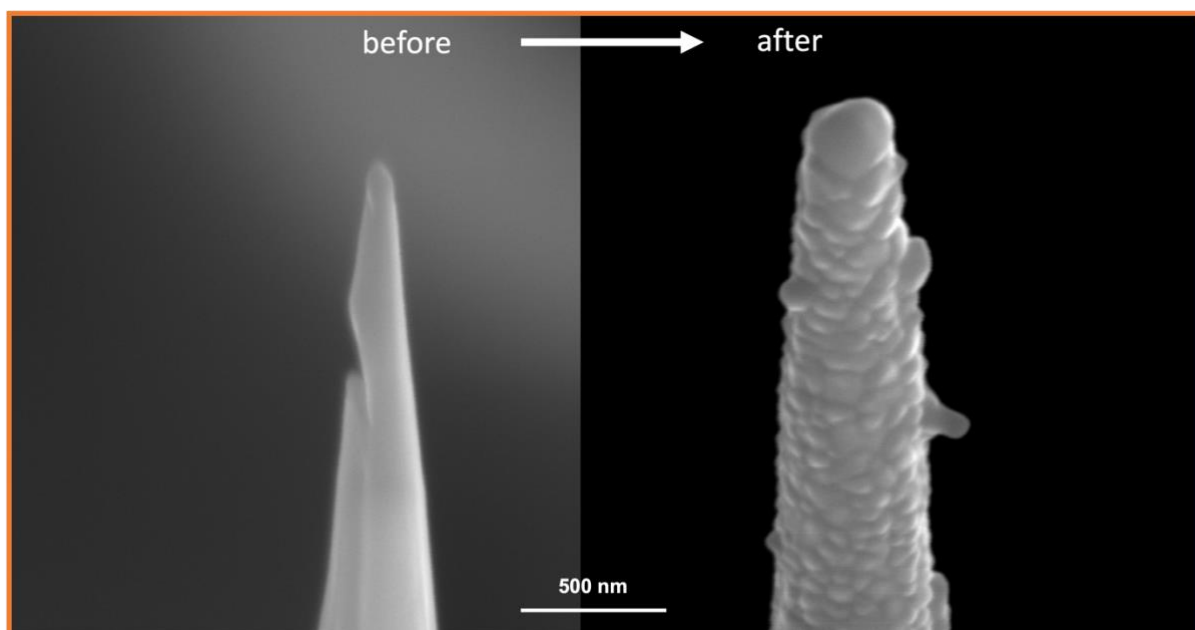


Figure S 5: Bismuth coating exhibits a very inhomogeneous coating and a very strong sputtering rate.

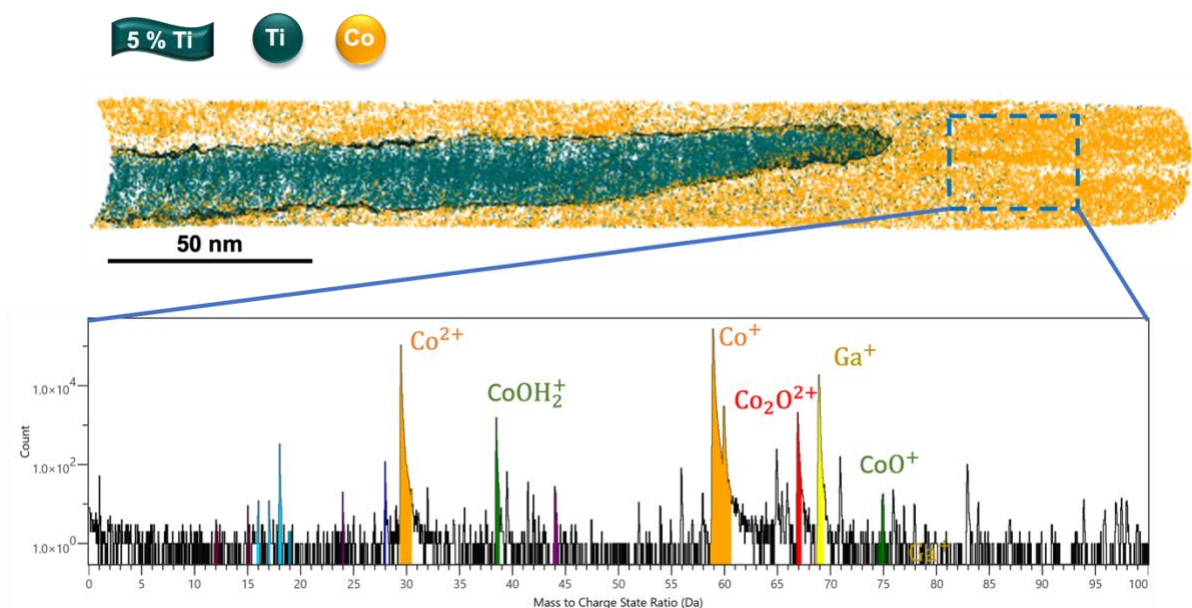


Figure S 6: Co coating shows a homogeneous coating around the specimen, the mass spectrum from the cobalt layer reveals that Co barely forms any oxides.

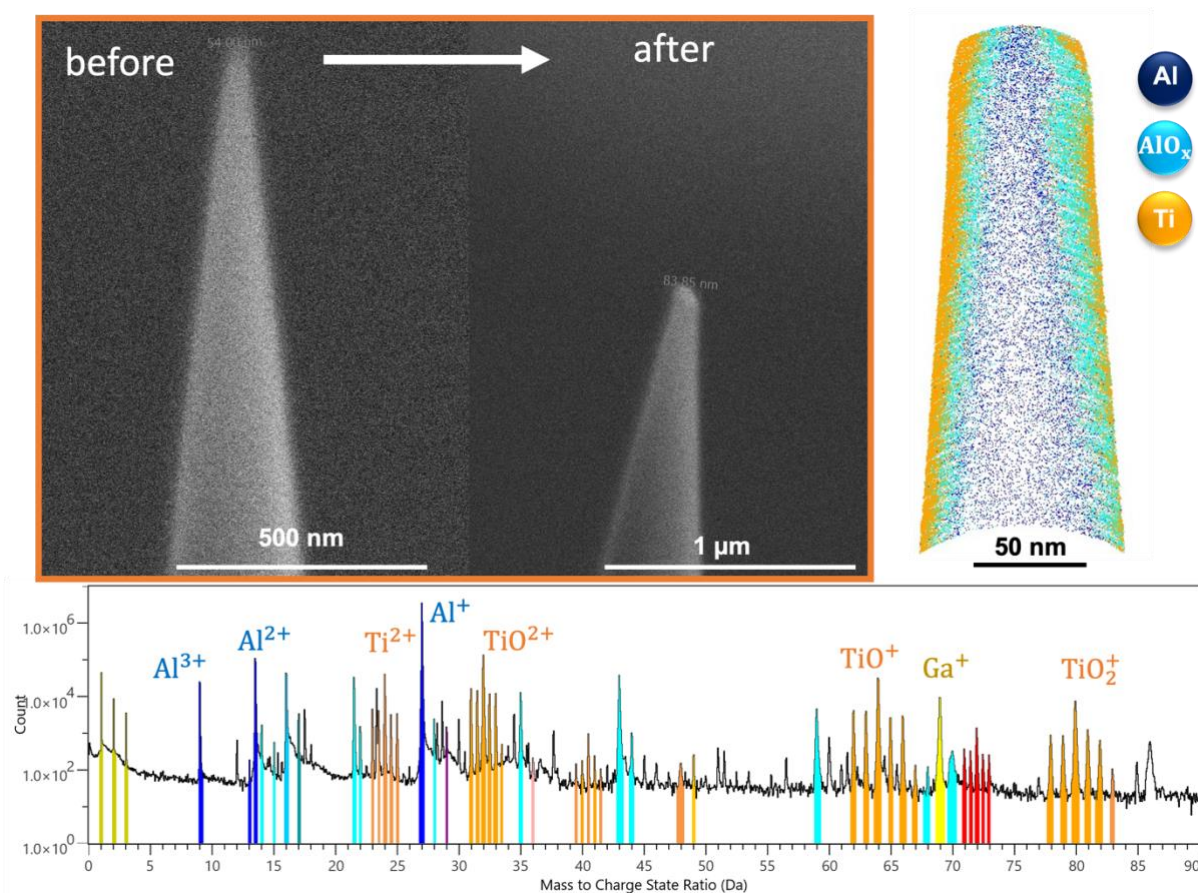


Figure S 7: Al specimen coated with Ti, indicates a uniform coating. However, the mass spectrum reveals that Ti has a very complex mass spectrum due to its isotopes and tendency to form oxides.